Spring 2015

Designing a Heat Sink for Lithium-ion Battery Packs in Electric Vehicles

Dylan Irvine
University of Akron Main Campus, dti3@zips.uakron.edu

Evan Foreman
The University Of Akron, etf4@zips.uakron.edu

Christopher B. Remington
The University Of Akron, cbr8@zips.uakron.edu

Aaron Jackson
The University Of Akron, adj29@zips.uakron.edu

Sam Endrizzi
The University Of Akron, swe2@zips.uakron.edu

Mechanical Engineering
Senior Design Report

Designing a Heat Sink for
Lithium-ion Battery Packs in Electric Vehicles

Faculty Supervisor: Dr. Siamak Farhad

Date: May 4, 2015

Group: Sam Endrizzi
Evan Foreman
Dylan Irvine
Aaron Jackson
Chris Remington

TABLE OF CONTENTS

ABSTRACT

This report addresses the concepts and implementation of fluid cooled heat sink designs for an electric or hybrid vehicle battery. To determine the battery's temperature and heat flux profile, testing was performed by measuring these values at multiple locations on a lithium-ion pouch battery using heat flux sensors and thermocouples during the charge and discharge cycles of the battery. Once the data was collected and analyzed, trendlines were fit to the heat flux data then used to create equations for the heat flux profile during the discharging stage. Each equation represented a specific region on the battery geometry. Four heat sink designs were modeled in COMSOL Multiphysics to optimize cooling. The third model concept (Model 3) was chosen as the best model because it cooled the battery to the lowest temperature with the lowest pressure drop.

INTRODUCTION

The Electric Vehicle (EV) market is expanding rapidly with the development of lithium-ion batteries. Components like battery packs and electric motors are now replacing gasoline-powered engines; regenerative braking and battery cooling systems are replacing alternators and radiators. Several automobile manufacturers have had trouble dealing with the amount of heat created by the discharging the batteries powering their vehicles, which results in overheating, non-functional vehicles.

Due to advantages such as high energy densities, rechargeability, and low self-discharge rates, lithium-ion batteries are the dominant technology for electric and hybrid vehicle applications. At present, automobile manufacturers are trying to design more durable battery packs to make electric and hybrid vehicles more attractive for

customers. When compared to other electronics such as cell phones and laptops, very large amounts of heat can be generated in a vehicle battery pack. This is due to the vehicles rapid acceleration and deceleration. Therefore, in order to increase the longevity and durability of the vehicle battery pack, the heat generated must be effectively dissipated in order to keep the battery temperature within the optimum range recommended by the manufacturer. With this in mind, the group set out to design an effective, fluid-cooled heat sink that, when placed in alternating order with battery pouches, would disperse the maximum amount of heat capable of being produced by the battery.

The objective of this project was to design an efficient heat sink (or fin) for a lithium-ion battery shown in Figure 1. The fin was to be inserted between batteries in the battery pack shown in Figure 2 in order to keep the hottest spot temperature in the battery pack within the optimum temperature range.

An efficient heat sink is a heat sink that is capable of keeping the battery temperature within the optimum range while maintaining a minimum weight, size, and cost. For this purpose, COMSOL software was used to simulate the heat dissipation from the designed heat sink. The heat dissipation by forced convections for water cooling was investigated in this project.

To successfully model and compare the heat sink designs, a specific battery was chosen to base the heat sink designs. For the chosen battery, experimental data and physical dimensions are required to accurately describe the heat flux model in COMSOL. Experimental surface heat flux data is gathered using heat flux sensors while cycling the battery using the BCS-815 battery cycler with a CC8 current collector

to measure the heat transfer rate over the surface (Figure 3). The heat flux sensors were strategically placed per Figure 4.

Before testing for the heat flux, the battery had to be activated. To activate the battery, it had to be fully charged and discharged 10 times. Then, to ensure the results were reproducible, the C-rate had to be found. The C-rate is important because it accurately describes the rate of charge or discharge for a battery. The C-rate was found using trial and error. The C-rate for the chosen battery, C1, was $18h^{-1}$. This means that a current of 18 amps will charge the fully depleted battery in one hour. C1, however, will not generate much heat when discharging. So a C-rate of 5C ($90h^{-1}$) was used to represent a worse-case scenario of aggressive acceleration.

During the 5C test, the heat flux sensors and thermocouples gathered data from the battery and then sent that data to a custom LabView VI (Figure 5). The VI then exported the data to a text file. The other side of the battery was also tested with the sensors positioned such that they applied to the same battery sections. Excel was used to analyze the data and create trendlines to find the average heat flux equation for each thermocouple (Figure 14).

LABVIEW

LabView 2013 was used to record all temperature and heat flux data. During the test we used sixteen different instrument channels. Nine of the channels were thermocouples for temperature measurements and seven were heat flux sensors. The two unpaired thermocouples were placed on the battery terminals. A Producer/Consumer loop setup was used to efficiently record the heat flux and temperature readings at a rate of 1Hz. LabView automatically converts the digital data

from the thermocouples to Celsius but the heat flux data was received as voltage. For this reason each heat flux sensor must be converted to $\frac{W}{m^2}$ by its unique sensitivity, given from the manufacturer. The sensitivities of the heat flux sensors were calculated from the English counterpart and then converted to metric. The reason for doing this and not using the manufacturer's sensitivity in metric is to mitigate the uncertainty.

The Labview VI is designed to instantaneously display temperature and heat flux data as the test is being run. If temperatures exceed a certain predetermined value, the test can be terminated. The collected data is also fed into a graph which accumulates all the data during the test so trends can be easily identified. Once the data is properly converted and displayed, the Labview VI then writes it to a text file. This data will be used for later calculations and modeling of the battery.

MODELING

When approaching the design of the heat sink, a "sandwiching" method was employed, where individual battery pouches would be placed between the fluid-cooled heat sinks in an alternating fashion (Figure 6). In this way, planes of symmetry can be defined through the center of the heat sinks. Due to this symmetric nature of the "sandwich," a model was able to be created of just one battery with half-sections of heat sink on either side.

The four half-heat sink models were created using PTC Creo Parametric 3D modeling software (Figure 7). The surface area of the battery used in this experiment had overall dimensions of 160 x 227mm, but the main concern was only the area of the battery that housed the cells and produced heat. So, disregarding the crimped areas and terminal tabs, the effective area of the battery was 153 x 204mm. With this

information, a 153 x 204mm rectangle was drawn and extruded to the desired thickness of the half-plate of the heat sink (2mm). The desired paths of the fluid flow channels were sketched onto the half-plate, and the Sweep function was utilized to create the desired flow channel cross-section along those paths. It was important that the cross-sections were swept as Surfaces, not Solids, so that when the half-plate was imported into COMSOL, the boundary between the fluid in the flow channel and the wall of the heat sink would be recognized. If swept as a Solid, COMSOL could not differentiate between the flow channels and the solid walls of the heat sink, and if swept as a Solid with the Remove Material option selected, there would be no domain for COMSOL to designate as the fluid in the flow channels.

The COMSOL Multiphysics modeling was an involved process. To begin, the Model Wizard was used and the 3D option was chosen. It must be recognized that there is a coupling of the heat transfer and fluid flow physics at work in the model. The heat flux of the battery is affected by the velocity, pressure, and temperature of the fluid flowing through the heat sink flow channels, which in-turn affects the heat flux of the battery. The assumption that all fluid flow would be laminar through the flow channels was made, so the **Conjugate Heat Transfer, Laminar Flow** physics was selected. This physics combines the **Heat Transfer in Solids** interface with the **Laminar Flow** interface. These two are the only physics that were considered in this modeling experiment. Any structural loading, vibration, or electrical aspects of the battery cooling process are irrelevant, and not considered.

The discharge of the battery from 3.6V to 2.5V at a rate of 5C took 12 minutes, or 720 seconds. In order to visualize the heat transfer and temperature changes over this period, a **Time-Dependent Study** was selected.

The half-plate was imported into COMSOL as an .igs file. A **Work Plane** was defined on the smooth surface of the plate (opposite the surface with the flow channels). On this plane, the 153 x 204mm area was split into seven rectangles, signifying the seven sections over which the seven heat flux sensors collected readings. These rectangles were then extruded the thickness of the battery, 7.25mm (Figure 8). The final step to complete the geometry of the model was to use the Mirror function to apply a half-plate to the other side of the extruded battery.

Using the **Explicit Selection** operator under the **Definitions** section of **Component 1**, the following explicits were defined: heat sink domain, flow channel domain, flow channel inlets and outlets, flow channel wall boundaries, symmetry plane boundaries, battery domain, and individual sections of the battery. In addition, for future use, the **Average** and **Maximum Component Couplings** were applied to the battery domain.

Two materials were selected from the **Materials Library** for the modeling. The fluid in the flow channels was defined as “Water, liquid” and the heat sink was defined as “Aluminum 6063-T83.” For the heat sink, 6063 Aluminum was chosen as it is a relatively cheap, common, material with a high thermal conductivity and high specific heat. The battery’s physical values were defined explicitly in the **Heat Transfer in Solids** section of COMSOL.

Only the flow channel domains were selected for the **Laminar Flow** section. The **Inlet** and **Outlet** boundaries were defined using **Laminar Inflow** and **Laminar Outflow**, respectively, as boundary conditions. At the inlet, the flow rate was defined explicitly as V_fluid_in in the definitions. At the outlet the pressure was assumed to be 0 psig for this study. The portion of the flow channels in contact with the aluminum half-plate were automatically defined as **Wall** conditions. Lastly, **Symmetry** was defined over the boundaries of the flow channels that were not in contact with the aluminum half-plate (Figure 9). It can be seen that if a second flow plate was placed against the first, there would be a plane of symmetry passing through the contact surface of the two plates.

For the **Heat Transfer in Solids** physics, all domains are selected because the heat created by the battery transfers through each domain present. The first step in defining the heat transfer physics was to define the battery's density, heat capacity, and thermal conductivity in **Heat Transfer in Solids 2** which applied only to the battery domain. The group was instructed to use values of $2100\ \frac{kg}{m^3}$ for density, $1400\ \frac{J}{kg*K}$ for heat capacity, $30\ \frac{W}{m*K}$ for thermal conductivity in the x- and y- directions, and thermal conductivity $1\ \frac{W}{m*K}$ in the z-direction. The reason the thermal conductivity in the z-direction is small relative to the x- and y- directions is that the battery itself is very thin in the z-direction (more than twenty times smaller than the x- and y- dimensions). Therefore, heat will be conducted much more easily in the x- and y- directions. **Heat Transfer in Fluids** was selected for the flow channel domains only, and the necessary properties for this condition were gathered from the **Material** settings. Since the volume of the flow channels was defined as liquid water, COMSOL attains density, thermal conductivity, specific heat ratios, etc. from the material definitions in the **Materials**

Library. The temperature at the flow channel inlet boundaries was constrained to the temperature $T\_fluid\_in = 293.15K$, or $20°C$. This ensured that the fluid entering the flow channels was at $20°C$, or ambient temperature. The **Outflow** boundary condition was defined at the flow channel outlets, meaning that the only heat transfer occurring across the boundary was by convection. **Symmetry** of heat transfer was defined across all boundaries on the plane of the half-plate and flow channels that would come into contact with another half-plate. Lastly, the **Heat Source** domain was used to define the heat generated by each of the seven sections of the battery. The equation $\frac{\dot{Q}"(t)_{top}+\dot{Q}"(t)_{bottom}}{battery\ thickness}$ was entered as a general heat source, where $\dot{Q}"(t)_{top}$ and $\dot{Q}"(t)_{bottom}$ are equations of the trendlines of the heat flux readings gathered through experimentation (Figure 13).

In order to save time, a simple **User-Controlled Mesh** was used. **Physics-Controlled** meshes, when built, returned average element quality values ranging between 0.3 and 0.45. However, by using a **Normal** sized **Free Tetrahedral** mesh, the number of mesh elements was greatly reduced, and the mesh quality increased to ~0.6 and greater.

For the **Time Dependent Study**, as mentioned before, the time range $t = (0;\ 5;\ 720)$ was used, where $t = 0$ is the beginning of the battery discharge, and $t = 720$ is the end of the discharge in seconds. A **Parametric Sweep** was used to vary V_fluid_in, the volumetric flow rate of liquid water through the flow channels. The values used were $0, 0.01, 0.1, 0.5, 1\ \frac{L}{min}$.

Post-processing is an important aspect of multiphysics modeling. The first step in post-processing was to define a **Volume Maximum** with the expression 'T' over the

Battery domain, a **Volume Maximum** with the expression 'p3' over the **Flow Channels** domain, and a **Volume Minimum** with the expression 'p3' over the **Flow Channels** domain. These **Derived Values** returned the maximum temperature in the battery, the maximum pressure in the flow channels, and the minimum pressure in the flow channels respectively at any time selection and/or volumetric flow parameter. For the purpose of determining the optimum flow channel design, the **Derived Values** are evaluated for all V_fluid_in values at $t = 720$, because this time is where the heat flux from the battery is the greatest. These three evaluations were saved as tables in the **Tables** section (Tables 1, 2, and 3). From there, **1D Plot Groups** could be created with **Table Graphs** to display the maximum and minimum pressures at the different volumetric flow rates (Figure 10). These are valuable because the pressure drops between the flow channel inlets and outlets for various flow rates and flow channel designs can be compared. The **Max/Min Line** function was used in the **Temperature 3D Plot Group** to designate the points of maximum and minimum temperatures. Another 3D plot group was created and a **Mesh Plot** was chosen—this displayed the mesh quality plots (Figure 11). Lastly, under **Export**, **Animation** was chosen. This allowed for the creation of a .gif movie that displayed the temperature changes in the battery/heat sink model from $t = 0$ to $t = 720$.

RESULTS AND DISCUSSION

The **Mesh Quality** plots show that the areas of lowest quality are in the flow channels (see Figure 11). The main concern of this modeling was the temperature of the battery; therefore, we can disregard the low quality mesh in the flow channels as long as the mesh quality is sufficiently high in the areas of the battery.

The aforementioned **Maximum Component Coupling**, defined in the **Definitions** section of **Component 1** with the operator name $maxop1$, is used as the **y-axis data** in a **Global Evaluation** in a 1D plot group to plot the battery's maximum temperature lines for each volumetric flow rate of each of the four heat sink models. Upon inspection of the four battery maximum temperature graphs, it is clear that Model 1 is not as functional as Models 2, 3, and 4 when it comes to dissipating heat from the battery (Figures 12). The battery is cooled to just over $25.5°C$ in Model 1 using its best case which is about $4°C$ less than the best case for every other model. Models 2, 3, and 4 all share similar temperature patterns—it is important to note that for each of these three models, the $0.5\ \frac{L}{min}$ and the $1\ \frac{L}{min}$ flow rates overlap each other for the majority of the 5C Discharge cycle, and keep the temperature at a minimum (Figures 12). For this reason, either $0.5\ \frac{L}{min}$ or $1\ \frac{L}{min}$ would be optimum. Models 3 and 4 have the lowest temperatures for these flow rates.

When considering the Maximum/Minimum Pressure vs. Flow Rate plots, it can be seen that the magnitude of the overall pressure drop is the difference between the value of the minimum pressure and the value of the maximum pressure at a given volumetric flow rate (see Figures 10). The pressure drop increases quadratically as the volumetric flow rate increases, which is expected due to Bernoulli's Equation, where velocity squared varies inversely with pressure. For this reason, the smallest flow rate possible is desired. From the plots, we see that Models 1, 3, and 4 all have pressure drops of roughly 0.12 psi. Since Model 1 had unimpressive cooling abilities, it will not be considered.

UNCERTAINTY ANALYSIS

To calculate the uncertainty of the heat flux data gathered, one must find all possible sources of error. The NI 9214, used as a thermocouple/heat flux sensor input module, has several sources of error, as outlined in the Specifications section of its user's manual. These include:

$Offset\ Error$: $U_O = 2\mu V\ typical, 8\mu V\ max$

$Gain\ Error$: $U_G = 0.03\%\ at\ 25℃$

$Input\ Noise$: $U_{IN} = 0.220\mu V$

$Resolution\ Uncertainty$: $U_{RES} = \frac{1}{2} Resolution = \frac{V_{Range}}{2^{bits}} = \frac{78.125\ V}{2^{24}} = 0.00233\mu V$

For values like the Gain Error, the maximum uncertainty would occur at the maximum heat flux value. These values can be found in Table 4.

The sensor uncertainty is obtained from the Omega Thin-Film Heat Flux Sensors Specification sheet. Nominal sensitivity is +/- 10%, so the uncertainty will be up to 10% of the sensitivity values used in the VI. These values were

$1.703\frac{\mu V}{\left(\frac{W}{m^2}\right)}$, $1.861\frac{\mu V}{\left(\frac{W}{m^2}\right)}$, $1.735\frac{\mu V}{\left(\frac{W}{m^2}\right)}$, $1.830\frac{\mu V}{\left(\frac{W}{m^2}\right)}$, $1.767\frac{\mu V}{\left(\frac{W}{m^2}\right)}$, $1.798\frac{\mu V}{\left(\frac{W}{m^2}\right)}$, $1.767\frac{\mu V}{\left(\frac{W}{m^2}\right)}$

for sensors 1-7 respectively. For sensor 1, the uncertainty would therefore be $0.1703\frac{\mu V}{\left(\frac{W}{m^2}\right)}$. The maximum uncertainty in μV clearly would occur at the maximum heat flux value (Found in Table 4).

$Max\ Sensor\ Uncertainty$: $U_S = 10\%\ of\ Nominal\ Sensitivity * Max\ Heat\ Flux\ Reading$

The following is the calculation of uncertainty for Sensor 1. Calculations of uncertainty for all other sensors are conducted in the same manner:

Sensor Uncertainty: $U_{s1,TOP} = 0.10 * 1.703 \frac{\mu V}{\left(\frac{W}{m^2}\right)} * 367.587 \frac{W}{m^2} = 62.600 \mu V$

$U_{s1,BOTTOM} = 0.10 * 1.703 \frac{\mu V}{\left(\frac{W}{m^2}\right)} * 392.836 \frac{W}{m^2} = 66.900 \mu V$

Offset Error: $U_O = 8 \mu V$

Gain Error: $U_{G1,TOP} = 0.0003 * 367.587 \frac{W}{m^2} * 1.703 \frac{\mu V}{\left(\frac{W}{m^2}\right)} = 0.01878 \mu V$

$$U_{G1,BOTTOM} = 0.0003 * 392.836 \frac{W}{m^2} * 1.703 \frac{\mu V}{\left(\frac{W}{m^2}\right)}$$

$$= 0.02007 \mu V$$

Input Noise: $U_{IN} = 0.220 \mu V$

Resolution Uncertainty: $U_{RES} = 0.00233 \mu V$

Max Total Uncertainty:

$$U_{1,Top,Total} = \sqrt{{U_{s1,TOP}}^2 + {U_O}^2 + {U_{G1,TOP}}^2 + {U_{IN}}^2 + {U_{RES}}^2}$$

$$= \sqrt{62.600 \mu V^2 + 8 \mu V^2 + 0.01878 \mu V^2 + 0.220 \mu V^2 + 0.00233 \mu V^2}$$

$$= 63.1095 \mu V \left(\frac{1}{1.703 \frac{\mu V}{\left(\frac{W}{m^2}\right)}} \right) = \pm 37.0578 \frac{W}{m^2}$$

$$U_{1,Bottom,Total} = \sqrt{{U_{s1,BOTTOM}}^2 + {U_O}^2 + {U_{G1,BOTTOM}}^2 + {U_{IN}}^2 + {U_{RES}}^2}$$

$$= \sqrt{66.900\mu V^2 + 8\mu V^2 + 0.02007\mu V^2 + 0.220\mu V^2 + 0.00233\mu V^2}$$

$$= 67.377\mu V \left(\frac{1}{1.703 \frac{\mu V}{\left(\frac{W}{m^2}\right)}} \right) = \pm 39.5637 \frac{W}{m^2}$$

CONCLUSIONS

Models 3 and 4 were determined to be the most viable options at flow rates of $0.5\ \frac{L}{min}$ or $1\ \frac{L}{min}$. After calculating the actual pressure drops for each flow rate from the derived values in COMSOL, it was determined that Model 3 had the smallest pressure drop at a flow rate of $0.5\ \frac{L}{min}$. Model 3, therefore, is the optimum heat sink design.

Using Model 3, it was found that the $0.5\ \frac{L}{min}$ flow rate was the optimal flow rate because the difference in temperature at $1\ \frac{L}{min}$ is negligible. Additionally, it was inferred that Model 3 reduced the temperature well and had the smallest pressure drop because it had wider channels and more passes over the battery than the other designs.

If this experiment were to be done over again, a few changes might make the results more reliable: using different thermal paste or adhesive thermal paste between the sensors and the battery, placing the sensors in the middle of the areas designated in COMSOL, and/or placing sensors on the front and back of the battery so that they do not need moved between data collections of front and back. The last option would allow for fewer tests in a shorter amount of time.

REFERENCES

Cespedes, Randy. *National Instruments Support* Evan Foreman. 16 April 2015. Telephone.

Dorfi, Dr. Hans. *Measurements Course ME483*. 8 March 2015. <http://gozips.uakron.edu/~dorfi/>.

"NI 9214 16-Channel Isothermal Thermocouple Input Module." 2015. *National Instruments.* Internet. 3 May 2015. <http://www.ni.com/pdf/manuals/375138b.pdf>.

"Thin Film Heat Flux Sensor." 2015. *Omega.* Internet. 3 May 2015. <http://www.omega.com/temperature/pdf/HFS-3_HFS-4.pdf>.

LIST OF SYMBOLS

V_fluid_in – input volumetric flowrate in $\frac{L}{min}$

T_fluid_in – input fluid temperature in K

t – time in seconds

$\dot{Q}"(t)$ – heat flux $\frac{W}{m^2}$

APPENDIX

Figure 1: A commercial lithium-ion battery designed for hybrid electric vehicles

Figure 2: A typical lithium-ion battery pack for hybrid electric vehicles

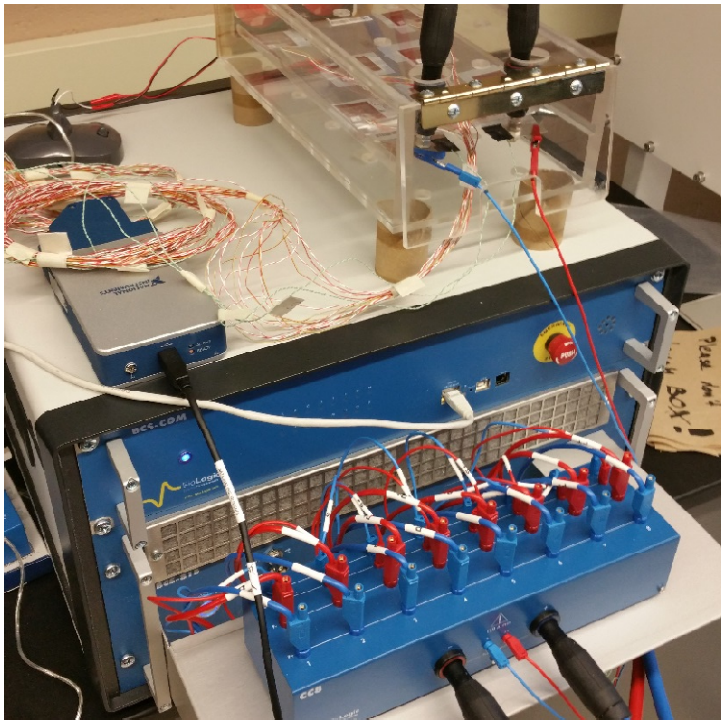

Figure 3: BCS-815 battery cycler with CC8 current collector

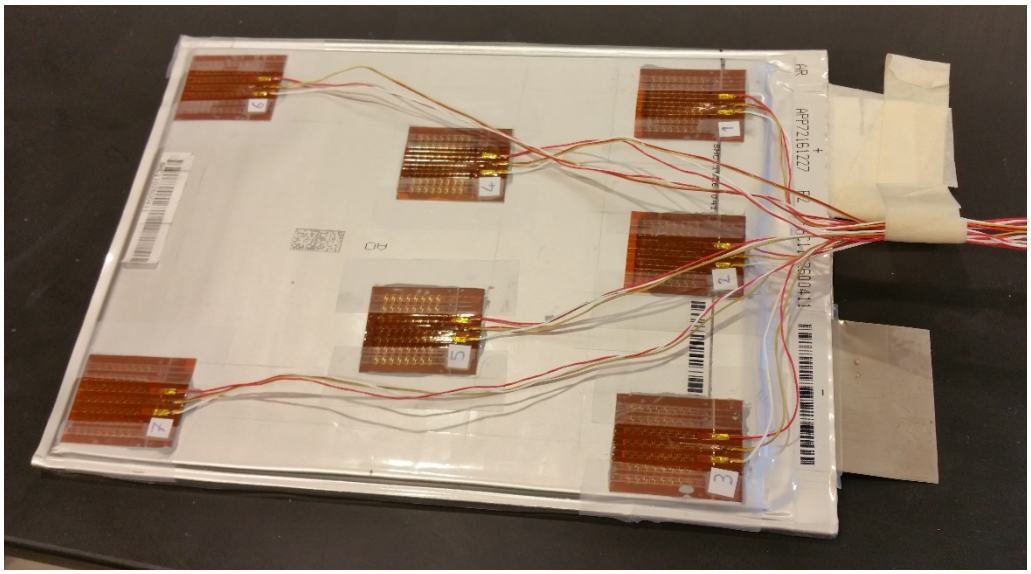

Figure 4: Sensor placement on battery

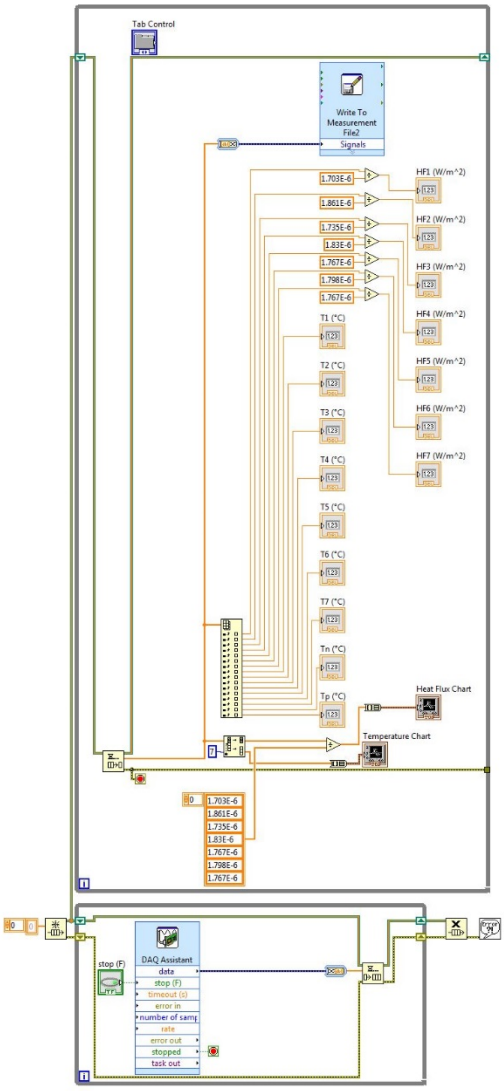

Figure 5: LabView VI

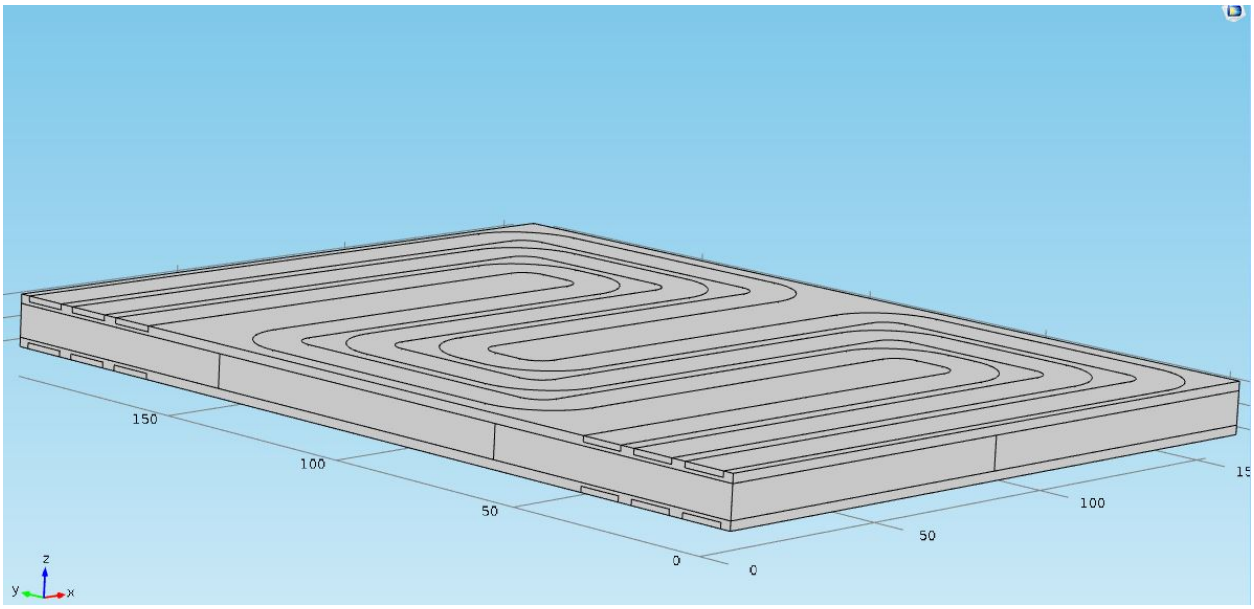

Figure 6: Sandwiching method

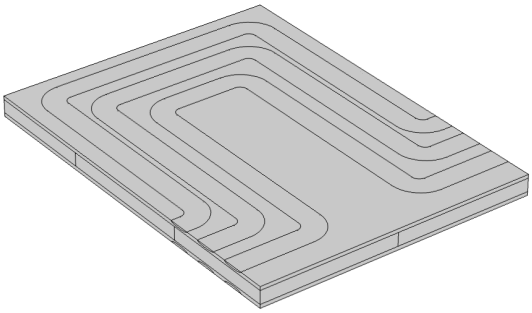

Model 1

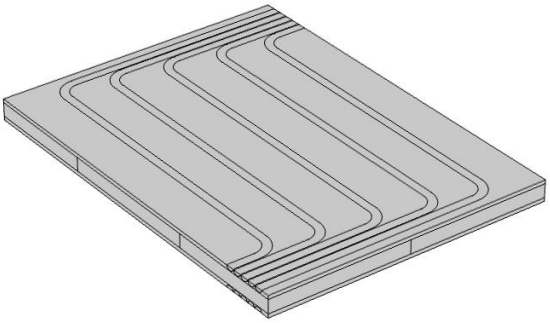

Model 2

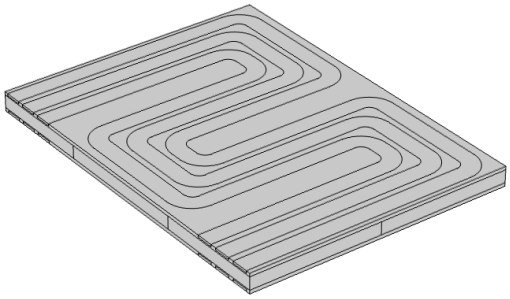

Model 3

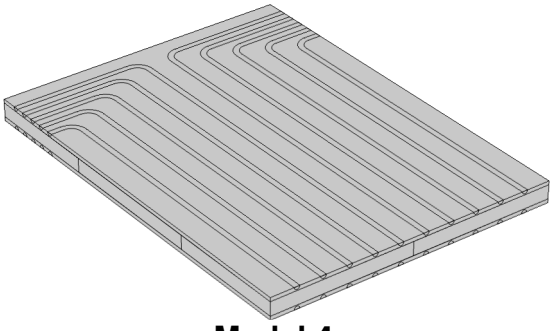

Model 4

Figure 7: Four Models

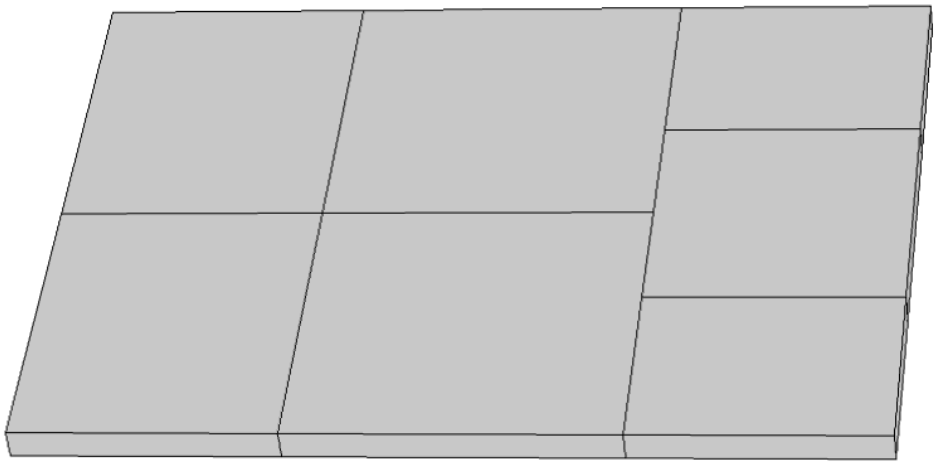

Figure 8: Battery sections

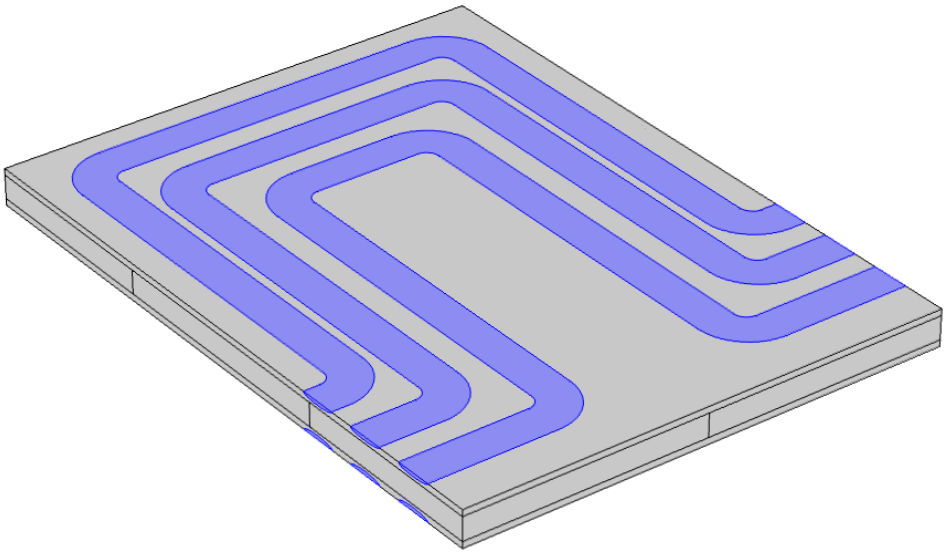

Figure 9: Flow channel symmetry boundaries

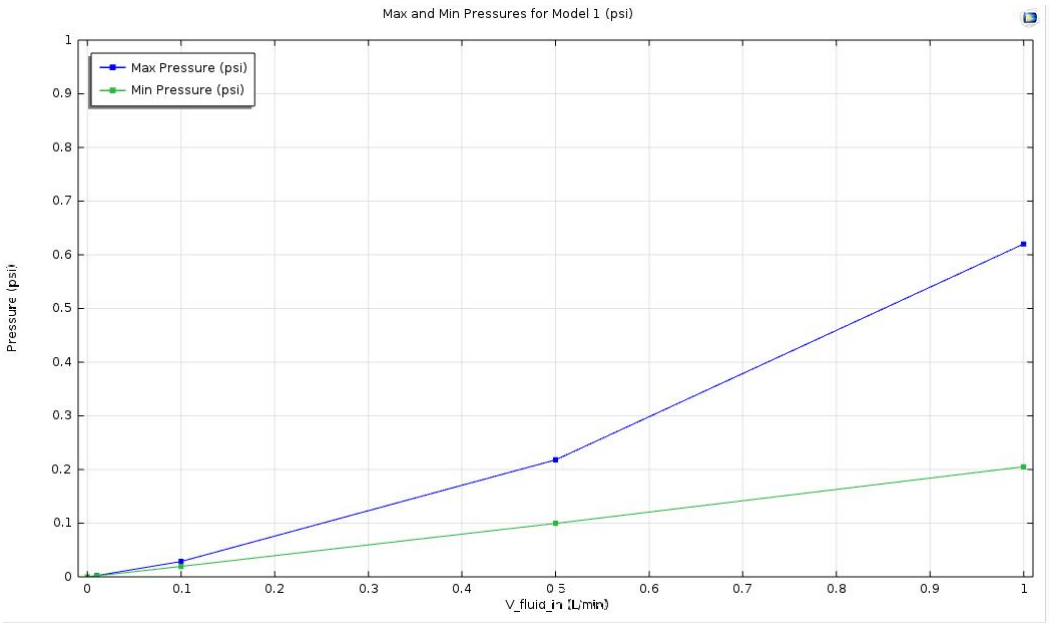

Figure 10 - Model 1: Pressure graph

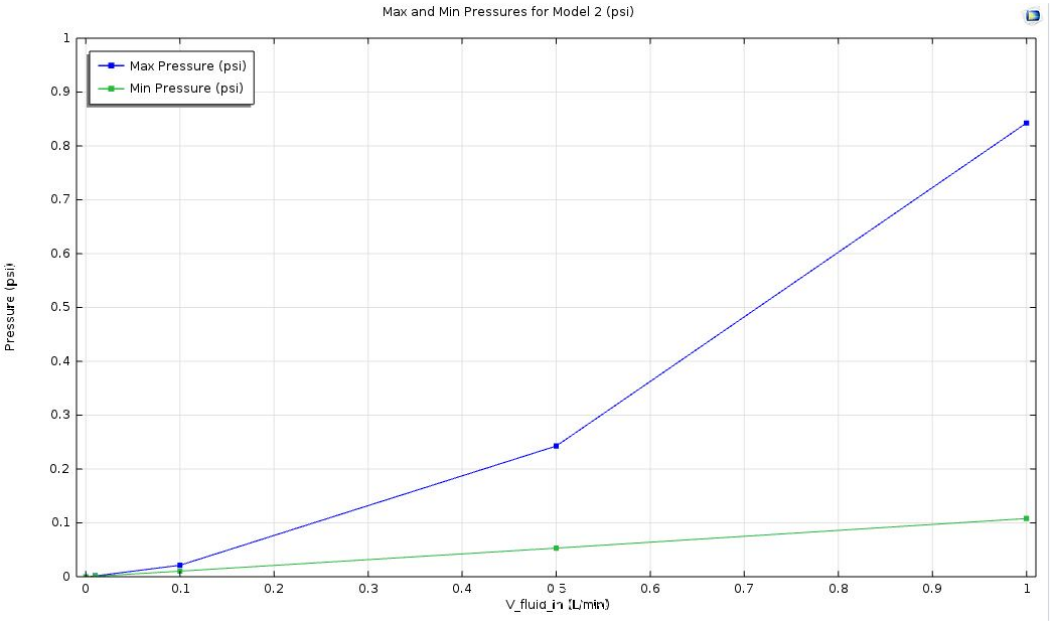

Figure 10 - Model 2: Pressure graph

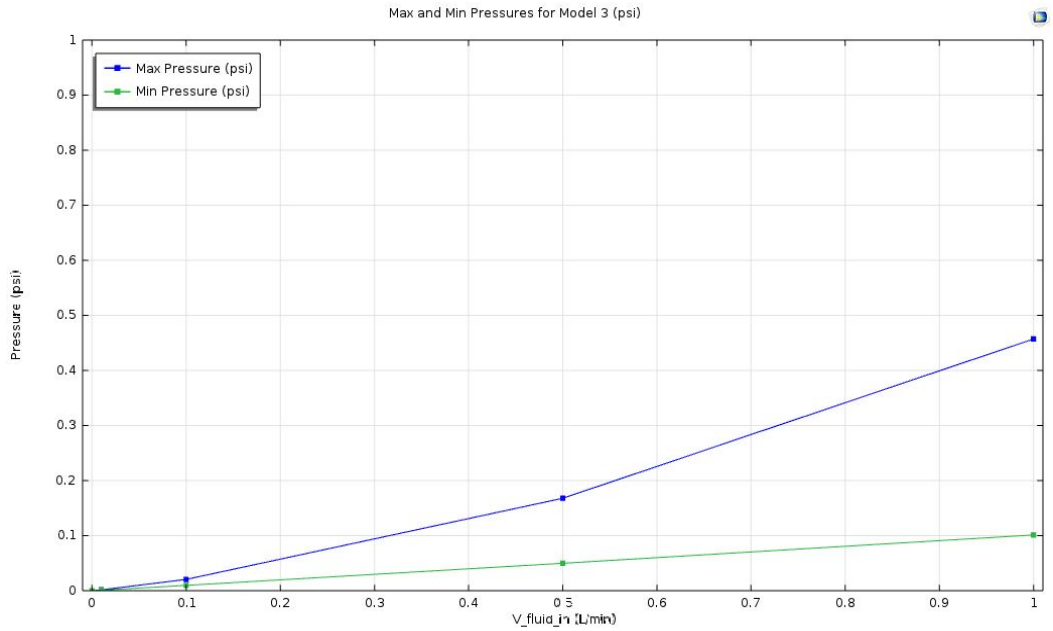

Figure 10 - Model 3: Pressure graph

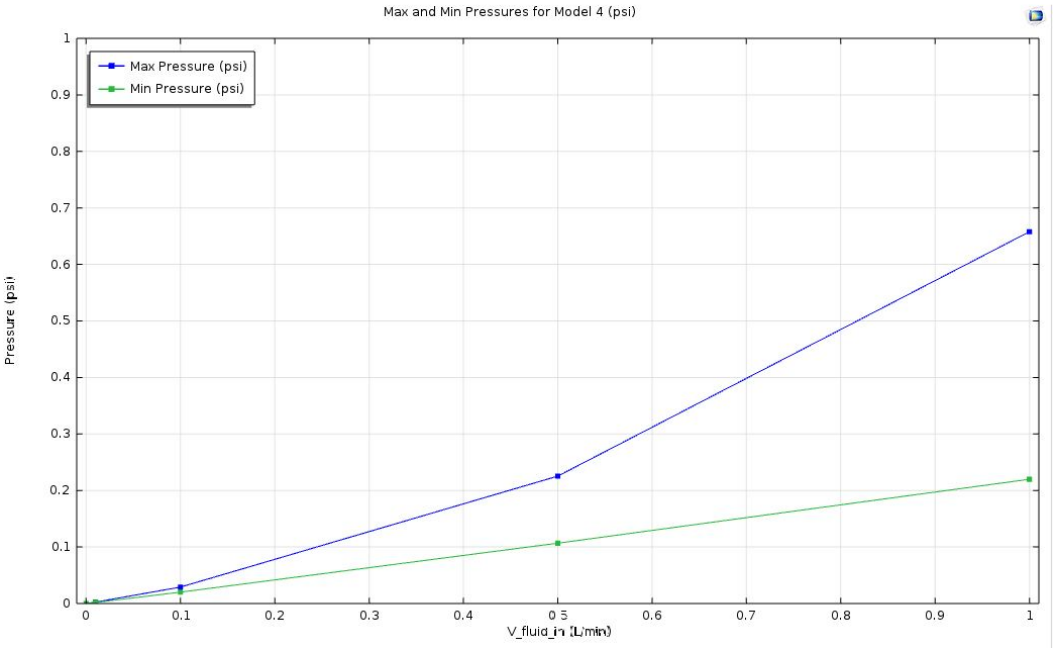

Figure 10 - Model 4: Pressure graph

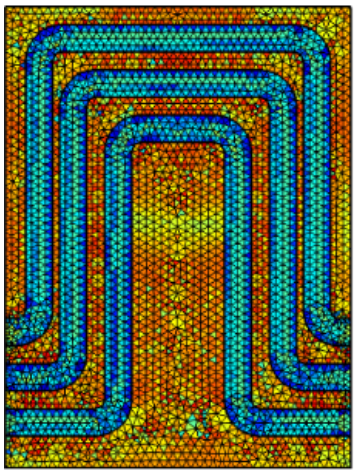

Model 1

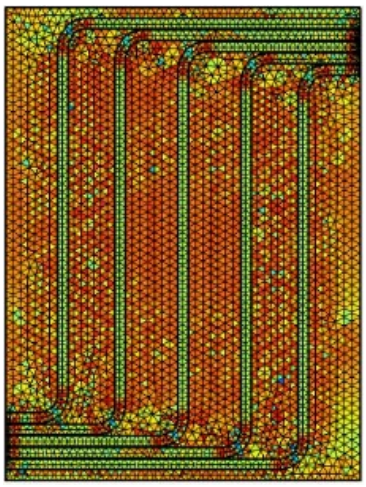

Model 2

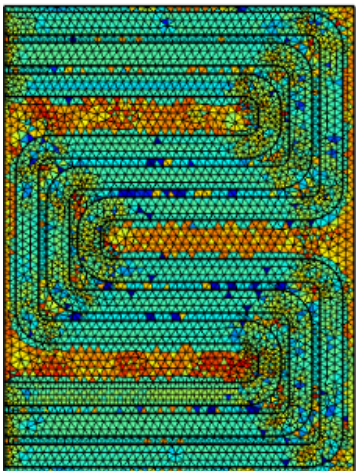

Model 3

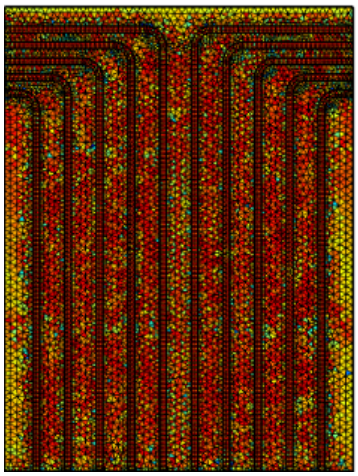

Model 4

Figure 11: Mesh quality plots

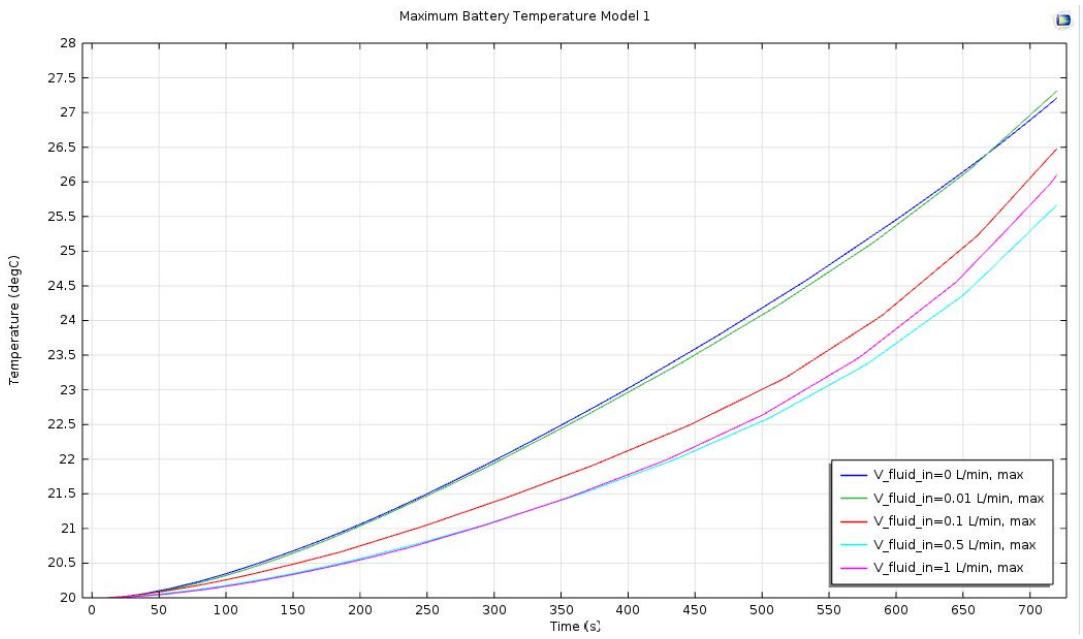

Figure 12 - Model 1: Temperature graph

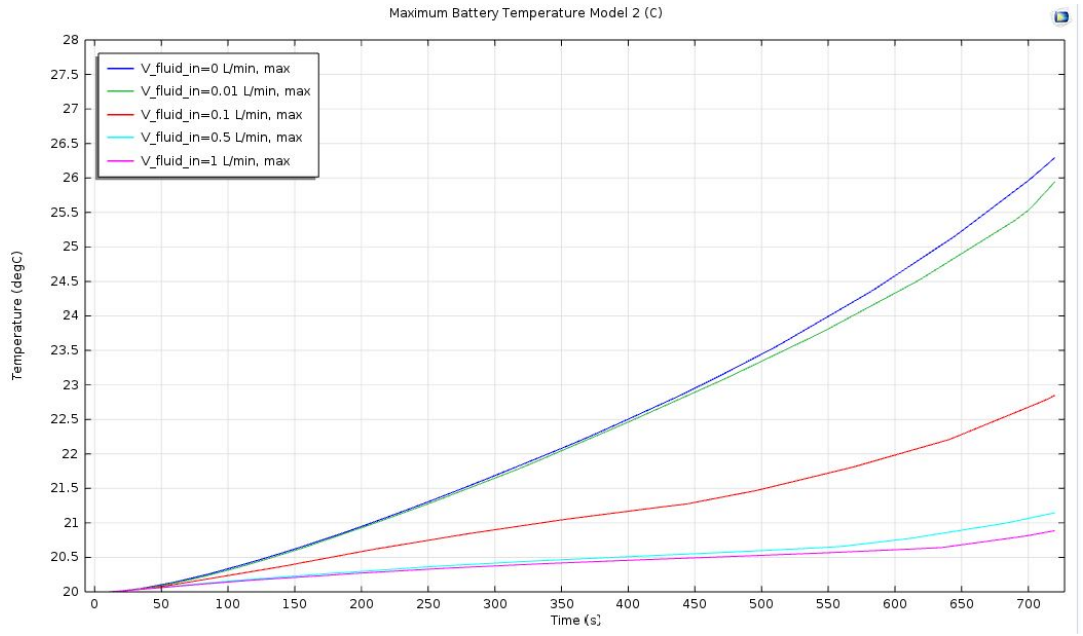

Figure 12 - Model 2: Temperature graph

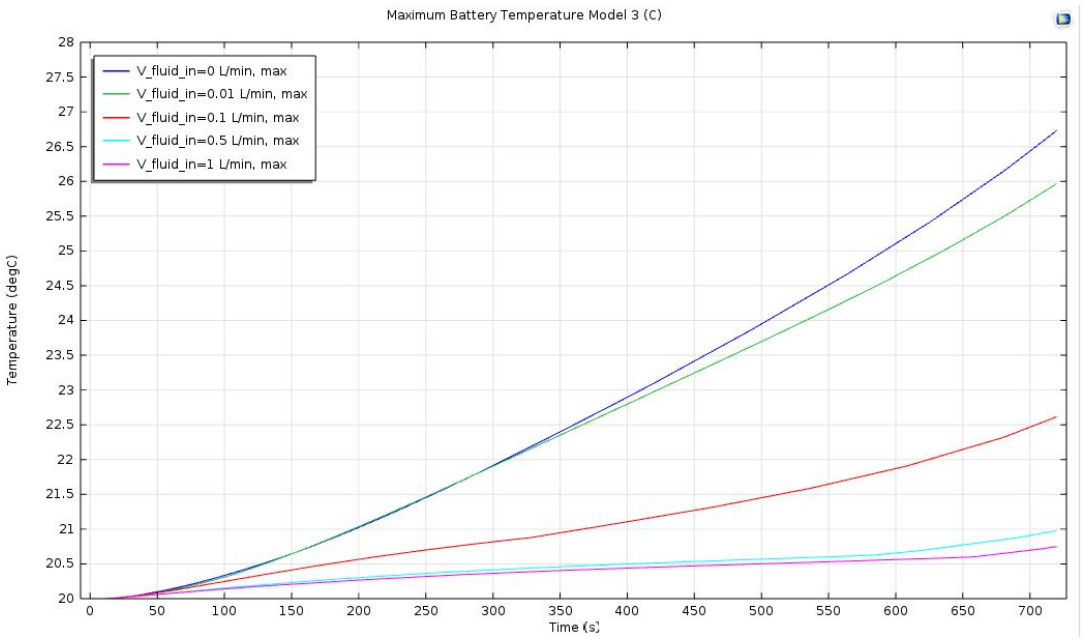

Figure 12 - Model 3: Temperature graph

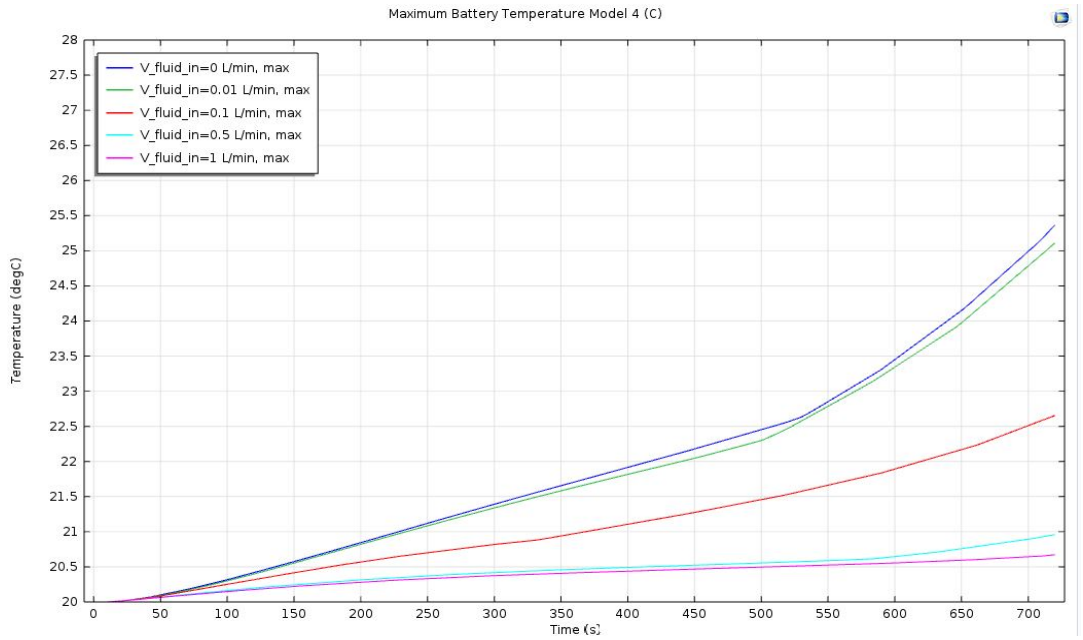

Figure 12 - Model 4: Temperature graph

Sensor 1 TOP	$Q"(t) = -6 * 10^{-7}t^3 + 0.001t^2 - 0.8028t + 17.552$
Sensor 1 BOTTOM	$Q"(t) = -2 * 10^{-6}t^3 + 0.002t^2 - 1.0361t + 4.992$
Sensor 1 Average Equation	$Q"(t) = -1.3 * 10^{-6}t^3 + 0.0015t^2 - 0.91945t + 11.272$
Sensor 2 TOP	$Q"(t) = -1 * 10^{-6}t^3 + 0.0018t^2 - 1.1136t + 9.1131$
Sensor 2 BOTTOM	$Q"(t) = -3 * 10^{-6}t^3 + 0.0033t^2 - 1.7419t + 8.0333$
Sensor 2 Average Equation	$Q"(t) = -2 * 10^{-6}t^3 + 0.00255t^2 - 1.42775t + 8.5732$
Sensor 3 TOP	$Q"(t) = -1 * 10^{-6}t^3 + 0.0014t^2 - 0.9622t + 21.303$
Sensor 3 BOTTOM	$Q"(t) = -8 * 10^{-7}t^3 + 0.0015t^2 - 1.3112t - 9.3224$
Sensor 3 Average Equation	$Q"(t) = -9 * 10^{-7}t^3 + 0.00145t^2 - 1.1367t + 5.9903$
Sensor 4 TOP	$Q"(t) = -2 * 10^{-6}t^3 + 0.0016t^2 - 0.6783t + 30.232$
Sensor 4 BOTTOM	$Q"(t) = -2 * 10^{-6}t^3 + 0.0015t^2 - 0.5717t + 25.181$
Sensor 4 Average Equation	$Q"(t) = -2 * 10^{-6}t^3 + 0.00155t^2 - 0.625t + 27.7065$
Sensor 5 TOP	$Q"(t) = -2 * 10^{-6}t^3 + 0.0015t^2 - 0.8067t + 27.612$
Sensor 5 BOTTOM	$Q"(t) = -1 * 10^{-6}t^3 + 0.0012t^2 - 0.5416t + 11.129$
Sensor 5 Average Equation	$Q"(t) = -1.5 * 10^{-6}t^3 + 0.00135t^2 - 0.67415t + 19.3705$
Sensor 6 TOP	$Q"(t) = -1 * 10^{-6}t^3 + 0.001t^2 - 0.4359t + 24.56$
Sensor 6 BOTTOM	$Q"(t) = -2 * 10^{-6}t^3 + 0.0015t^2 - 0.5622t + 22.839$
Sensor 6 Average Equation	$Q"(t) = -1.5 * 10^{-6}t^3 + 0.00125t^2 - 0.49905t + 23.6995$
Sensor 7 TOP	$Q"(t) = -9 * 10^{-7}t^3 + 0.0008t^2 - 0.4736t + 24.822$
Sensor 7 BOTTOM	$Q"(t) = -1 * 10^{-6}t^3 + 0.0013t^2 - 0.602t + 19.005$
Sensor 7 Average Equation	$Q"(t) = -9.5 * 10^{-7}t^3 + 0.00105t^2 - 0.5378t + 21.9135$

Figure 13: Average heat flux equations

Figures 14, a-h: Battery Heat Flux Graphs

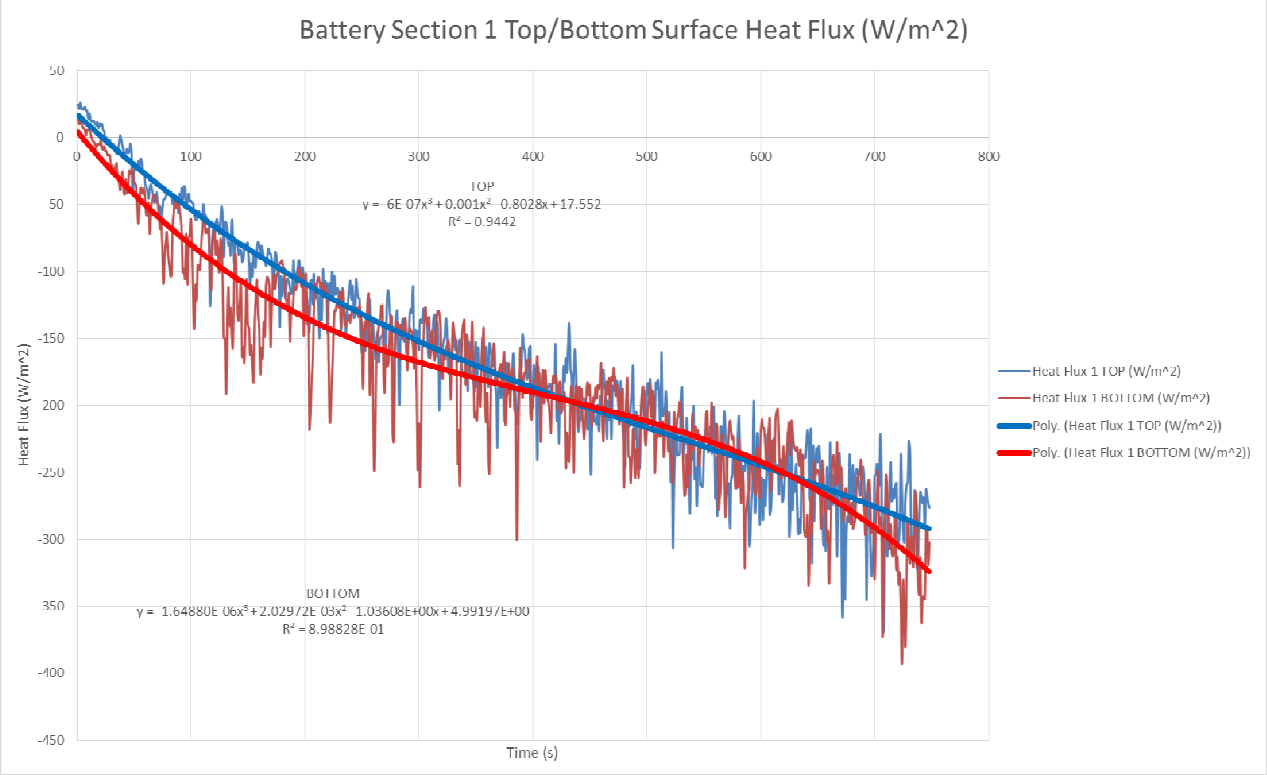

(A)

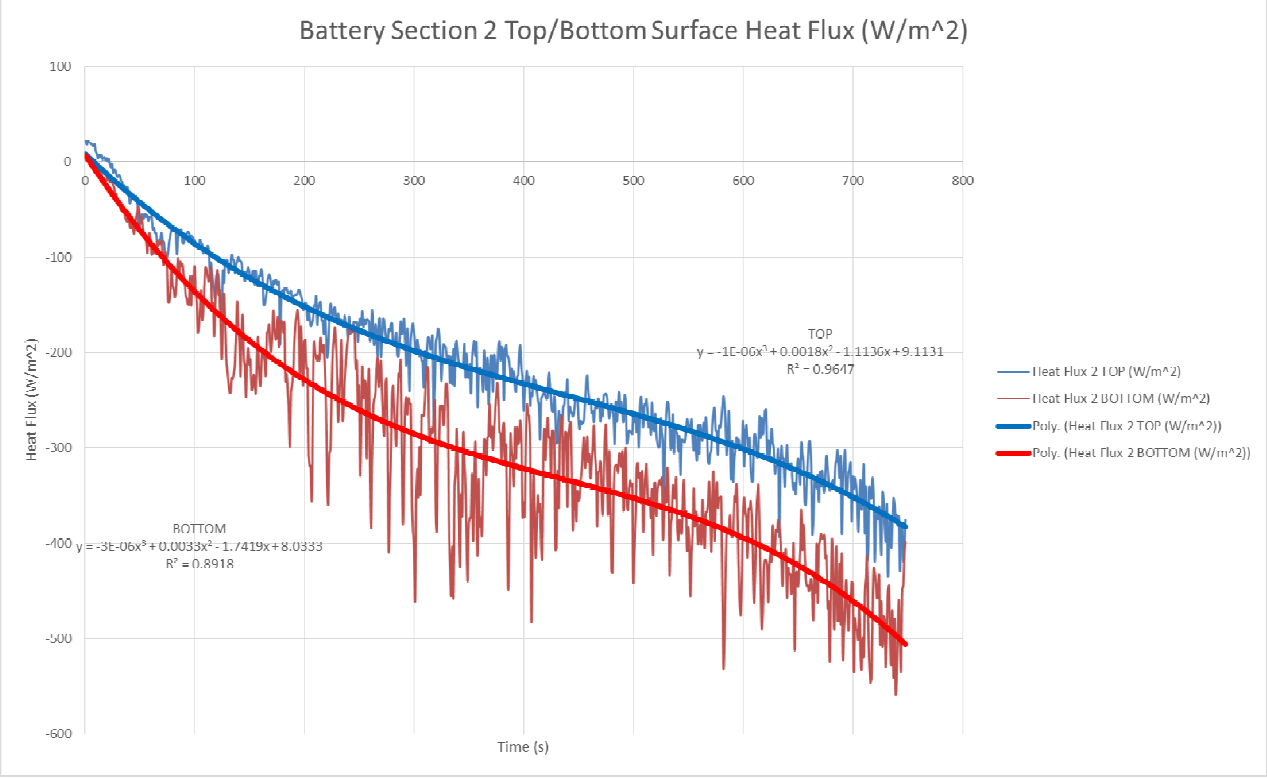

(B)

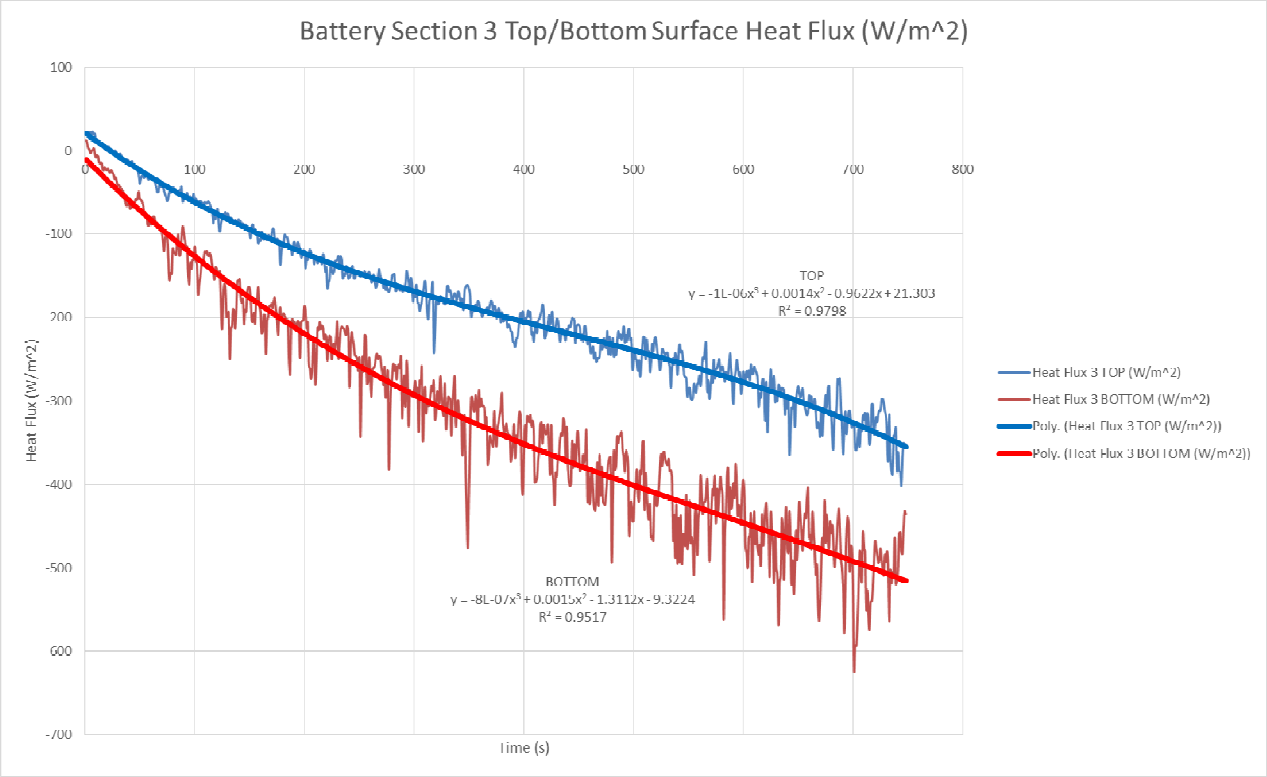
Battery Section 3 Top/Bottom Surface Heat Flux (W/m^2)
Heat Flux (W/m^2)
Time (s)
TOP
y = -1E-06x³ + 0.0014x² - 0.9622x + 21.303
R² = 0.9798
BOTTOM
y = -8E-07x³ + 0.0015x² - 1.3112x - 9.3224
R² = 0.9517
Heat Flux 3 TOP (W/m^2)
Heat Flux 3 BOTTOM (W/m^2)
Poly. (Heat Flux 3 TOP (W/m^2))
Poly. (Heat Flux 3 BOTTOM (W/m^2))

(C)

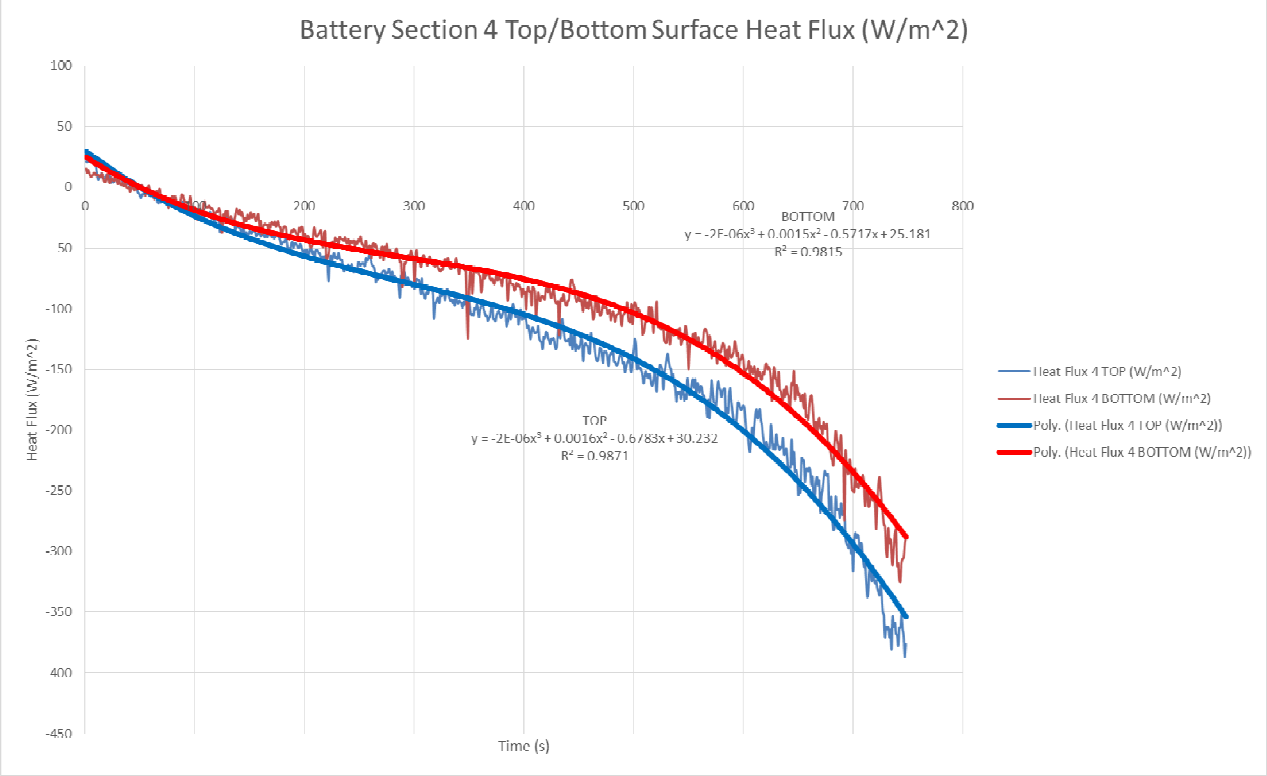
Battery Section 4 Top/Bottom Surface Heat Flux (W/m^2)
Heat Flux (W/m^2)
Time (s)
BOTTOM
y = -2E-06x³ + 0.0015x² - 0.5717x + 25.181
R² = 0.9815
TOP
y = -2E-06x³ + 0.0016x² - 0.6783x + 30.232
R² = 0.9871
Heat Flux 4 TOP (W/m^2)
Heat Flux 4 BOTTOM (W/m^2)
Poly. (Heat Flux 4 TOP (W/m^2))
Poly. (Heat Flux 4 BOTTOM (W/m^2))

(D)

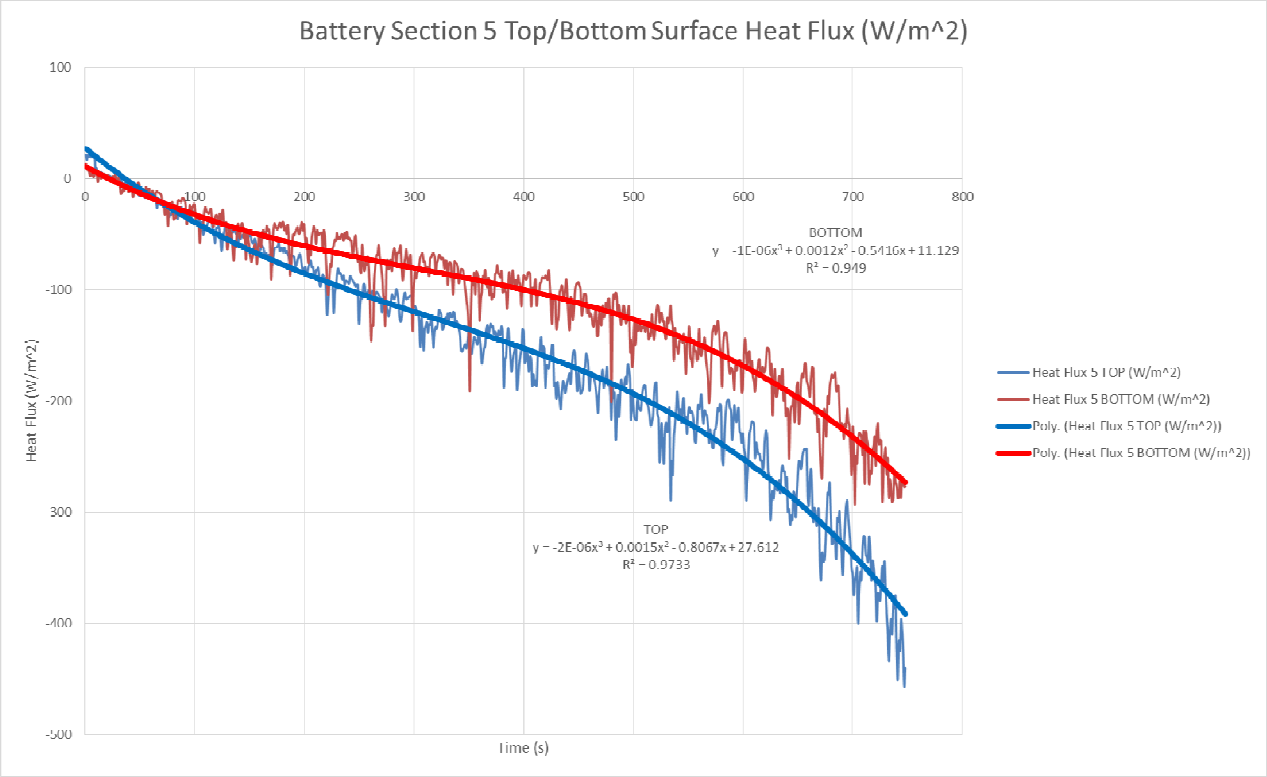
Battery Section 5 Top/Bottom Surface Heat Flux (W/m^2)
Heat Flux (W/m^2)
Time (s)
BOTTOM
y = -1E-06x³ + 0.0012x² - 0.5416x + 11.129
R² = 0.949
TOP
y = -2E-06x³ + 0.0015x² - 0.8067x + 27.612
R² = 0.9733
Heat Flux 5 TOP (W/m^2)
Heat Flux 5 BOTTOM (W/m^2)
Poly. (Heat Flux 5 TOP (W/m^2))
Poly. (Heat Flux 5 BOTTOM (W/m^2))

(E)

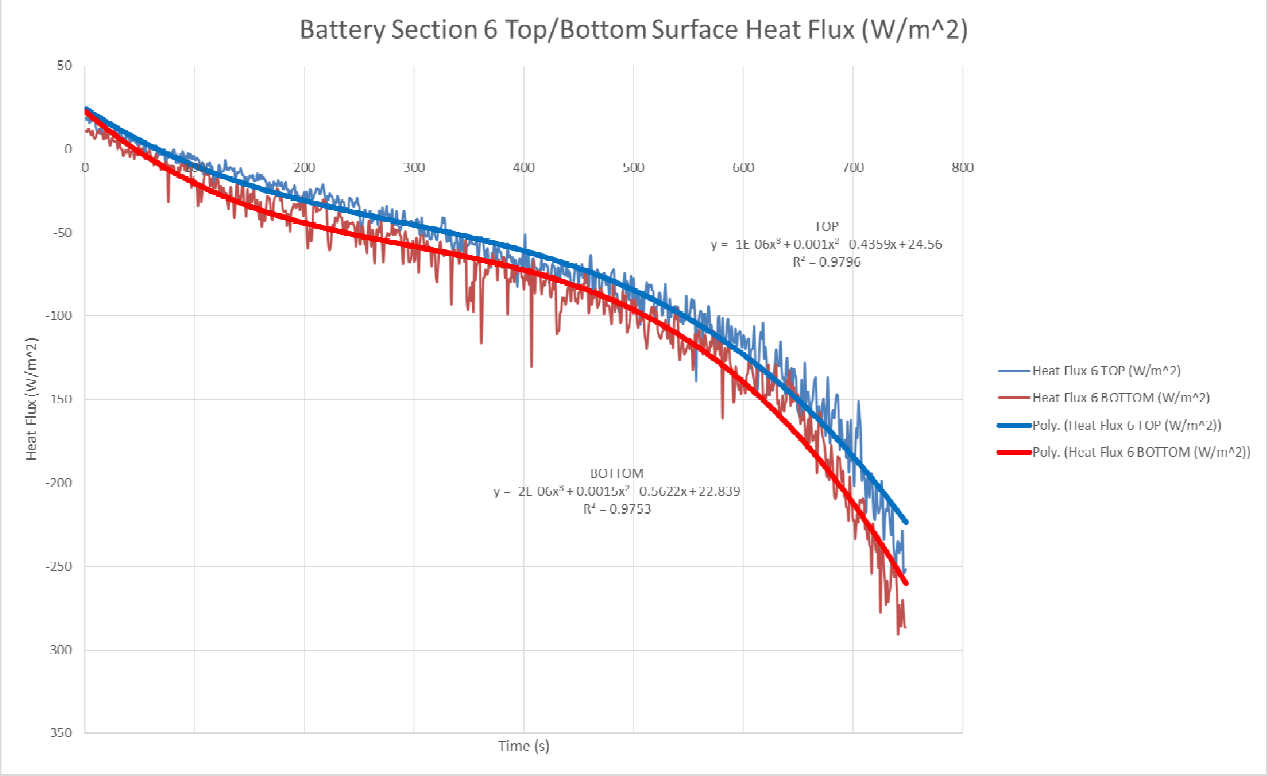
Battery Section 6 Top/Bottom Surface Heat Flux (W/m^2)
Heat Flux (W/m^2)
Time (s)
TOP
y = 1E-06x³ + 0.001x² - 0.4359x + 24.56
R² = 0.9796
BOTTOM
y = -2E-06x³ + 0.0015x² - 0.5622x + 22.839
R² = 0.9753
Heat Flux 6 TOP (W/m^2)
Heat Flux 6 BOTTOM (W/m^2)
Poly. (Heat Flux 6 TOP (W/m^2))
Poly. (Heat Flux 6 BOTTOM (W/m^2))

(F)

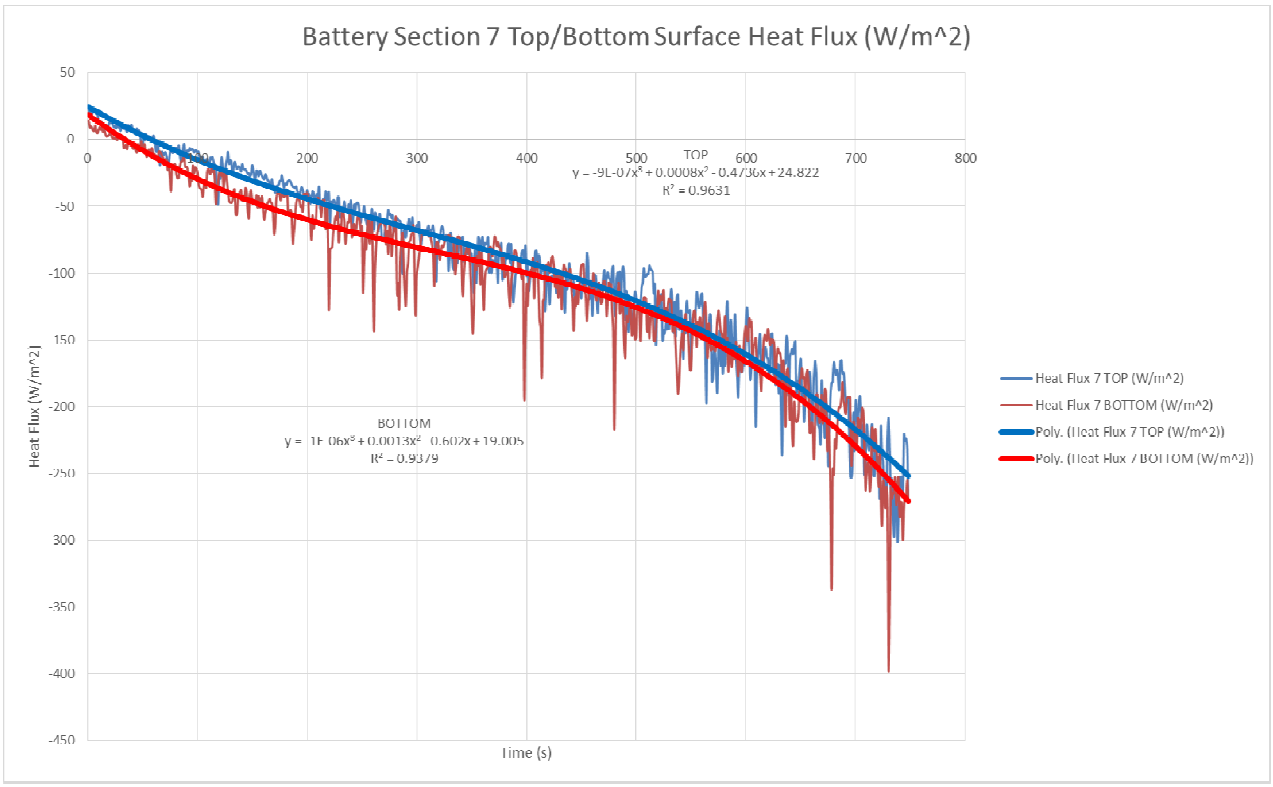
Battery Section 7 Top/Bottom Surface Heat Flux (W/m^2)
Heat Flux (W/m^2)
Time (s)
TOP
y = -9E-07x^3 + 0.0008x^2 - 0.4736x + 24.822
R^2 = 0.9631
BOTTOM
y = 1E-06x^3 + 0.0013x^2 - 0.602x + 19.005
R^2 = 0.9379
Heat Flux 7 TOP (W/m^2)
Heat Flux 7 BOTTOM (W/m^2)
Poly. (Heat Flux 7 TOP (W/m^2))
Poly. (Heat Flux 7 BOTTOM (W/m^2))

(G)

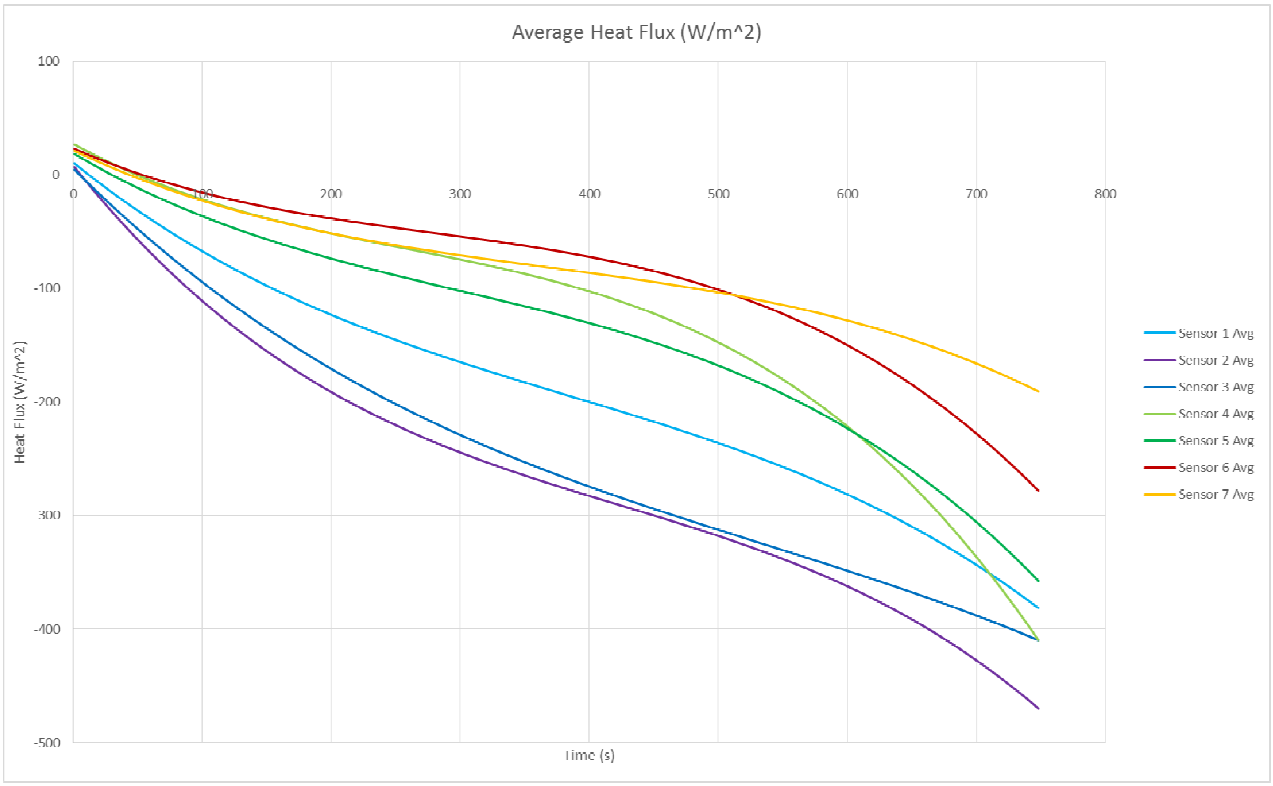
Average Heat Flux (W/m^2)
Heat Flux (W/m^2)
Time (s)
Sensor 1 Avg
Sensor 2 Avg
Sensor 3 Avg
Sensor 4 Avg
Sensor 5 Avg
Sensor 6 Avg
Sensor 7 Avg

(H)

V_fluid_in (L/min)	t (s)	Max Temperature (degC)
0.0000	720.00	26.731
0.010000	720.00	25.968
0.10000	720.00	22.615
0.50000	720.00	20.977
1.0000	720.00	20.750

Table 1: Max battery temperature at different flow rates

V_fluid_in (L/min)	t (s)	Min Pressure (psi)
0.0000	720.00	1.0425E-6
0.010000	720.00	9.2426E-4
0.10000	720.00	0.0096171
0.50000	720.00	0.049759
1.0000	720.00	0.10116

Table 2: Minimum pressure in the flow channels of the battery

V_fluid_in (L/min)	t (s)	Max Pressure (psi)
0.0000	720.00	1.5191E-6
0.010000	720.00	0.0015220
0.10000	720.00	0.020435
0.50000	720.00	0.16780
1.0000	720.00	0.45711

Table 3: Maximum pressure in the flow channels of the battery

Table 4: Uncertainty analysis

	Offset Error (μV)	Gain Error (μV)	Input Noise (μV)	Resolution Ur (μV)
5	8	0.01878	0.220	
7	8	0.02421	0.220	
6	8	0.02088	0.220	
8	8	0.02124	0.220	
7	8	0.02421	0.220	
5	8	0.01368	0.220	
3	8	0.01599	0.220	
9	8	0.02007	0.220	
5	8	0.03108	0.220	
1	8	0.03243	0.220	
5	8	0.01785	0.220	
8	8	0.01554	0.220	
3	8	0.01569	0.220	
0	8	0.021	0.220	

Team members (left to right):
Sam Endrizzi, Dylan Irvine, Chris Remington, Evan Foreman, Aaron Jackson